



**HAL**  
open science

# Characterization of the structure and cross-shore transport properties of a coastal upwelling filament using three-dimensional finite-size Lyapunov exponents

João Bettencourt, Vincent Rossi, Emilio Hernández-García, Martinho Marta-Almeida, Cristóbal López

## ► To cite this version:

João Bettencourt, Vincent Rossi, Emilio Hernández-García, Martinho Marta-Almeida, Cristóbal López. Characterization of the structure and cross-shore transport properties of a coastal upwelling filament using three-dimensional finite-size Lyapunov exponents. *Journal of Geophysical Research. Oceans*, 2017, 122 (9), pp.7433 - 7448. 10.1002/2017JC012700 . hal-01731121

**HAL Id: hal-01731121**

**<https://amu.hal.science/hal-01731121>**

Submitted on 31 Dec 2021

**HAL** is a multi-disciplinary open access archive for the deposit and dissemination of scientific research documents, whether they are published or not. The documents may come from teaching and research institutions in France or abroad, or from public or private research centers.

L'archive ouverte pluridisciplinaire **HAL**, est destinée au dépôt et à la diffusion de documents scientifiques de niveau recherche, publiés ou non, émanant des établissements d'enseignement et de recherche français ou étrangers, des laboratoires publics ou privés.

Copyright

## RESEARCH ARTICLE

10.1002/2017JC012700

## Key Points:

- Three-dimensional structure and hydrographic characteristics of an upwelling filament are analyzed using Lagrangian tools
- Low values of finite-size Lyapunov exponent evidence low dispersion and relatively homogeneous thermohaline properties inside the filament
- Lagrangian Coherent Structures delimit the filament, isolate it from surrounding waters, and match hydrographic gradients

## Correspondence to:

J. H. Bettencourt,  
jhbettencourt@protonmail.com

## Citation:

Bettencourt, J. H., V. Rossi, E. Hernández-García, M. Marta-Almeida, and C. López (2017), Characterization of the structure and cross-shore transport properties of a coastal upwelling filament using three-dimensional finite-size Lyapunov exponents, *J. Geophys. Res. Oceans*, 122, 7433–7448, doi:10.1002/2017JC012700.

Received 13 JAN 2017

Accepted 17 AUG 2017

Accepted article online 25 AUG 2017

Published online 15 SEP 2017

## Characterization of the structure and cross-shore transport properties of a coastal upwelling filament using three-dimensional finite-size Lyapunov exponents

João H. Bettencourt<sup>1,2</sup> , Vincent Rossi<sup>1,3</sup> , Emilio Hernández-García<sup>1</sup> ,  
Martinho Marta-Almeida<sup>4</sup> , and Cristóbal López<sup>1</sup>

<sup>1</sup>IFISC(CSIC-UIB), Instituto de Física Interdisciplinar y Sistemas Complejos, Campus Universitat de les Illes Balears, Palma de Mallorca, Spain, <sup>2</sup>Now at LEGOS-OMP, Toulouse, France, <sup>3</sup>Now at Mediterranean Institute of Oceanography, CNRS, Aix Marseille Univ., Univ. Toulon, IRD, Marseille, France, <sup>4</sup>Instituto Español de Oceanografía, Centro Oceanográfico A Coruña, A Coruña, Spain

**Abstract** The three-dimensional structure, dynamics, and dispersion characteristics of a simulated upwelling filament in the Iberian upwelling system are analyzed using Lagrangian tools. We used a realistic regional simulation of the western Iberian shelf which is concomitant with an in situ oceanographic campaign that surveyed the area. We compute 3-D fields of finite-size Lyapunov exponents (FSLE) from 3-D velocity fields and extract the field's ridges to study the spatial distribution and temporal evolution of the Lagrangian Coherent Structures (LCSs) evolving around the filament. We find that the most intense curtain-like LCSs delimit the boundaries of the whole filamentary structure whose general properties match well the observations. The filament interior is characterized by small dispersion of fluid elements. Furthermore, we identify a weak LCS separating the filament into a warmer vein and a colder filament associated with the interaction of a mesoscale eddy with the upwelling front. The cold upwelled water parcels move along the filament conserving their density. The filament itself is characterized by small dispersion of fluid elements in its interior. The comparison of LCSs with potential temperature and salinity gradient fields shows that the outer limits of the filament coincide with regions of large hydrographic gradients, similar to those observed, explaining the isolation of the interior of the filament with the surrounding waters. We conclude that the Lagrangian analysis used in this work is useful in explaining the dynamics of cross-shore exchanges of materials between coastal regions and the open ocean due to mesoscale processes.

### 1. Introduction

Mesoscale filamental structures are ubiquitous features of the ocean and more particularly in the coastal ocean, in which they play a key role in cross-shelf exchanges of water masses. In upwelling regions, this role of filaments is of even a greater importance due to the intense biological productivity near-shore and their fertilizing role of the adjacent oligotrophic ocean [Álvarez-Salgado *et al.*, 2007]. In the Iberian Peninsula Upwelling System, mesoscale processes, rather than large-scale variability, are the dominant factors controlling the strength of the coastal upwelling [Relvas *et al.*, 2009] and the response of its associated ecosystem [Rossi *et al.*, 2013a]. The regional oceanography reveals a series of mesoscale structures such as jets, meanders, eddies, and upwelling filaments, superimposed on the large-scale seasonal patterns [Peliz *et al.*, 2002]. From a biological perspective, dynamics with spatial scales of 10–100 km are determinant for the control of larval retention and dispersal [Queiroga *et al.*, 2007] and more generally, of the distribution and variability of marine planktonic communities [Relvas *et al.*, 2007; Cravo *et al.*, 2010; Rossi *et al.*, 2013a; Hernández-Carrasco *et al.*, 2014].

In the late Spring/early Summer, predominantly northerly coastal winds start to blow in the western Iberian Peninsula, driving an offshore Ekman transport in the surface layers that forces the upwelling of colder, nutrient-rich, subsurface waters along the coast. The depth of the surface Ekman layer usually ranges 20–60 m and the upwelled waters come from as deep as 200 m in a 10–20 km wide strip of coastal upwelling with vertical velocities of the order of  $\sim 10 \text{ m d}^{-1}$  [Barton, 2001]. Shortly after the initiation of the upwelling-favorable winds, large filaments start to develop, associated with strong offshore currents of  $\sim 0.5 \text{ m s}^{-1}$

that can extend more than 200 km [Haynes *et al.*, 1993; Relvas *et al.*, 2007; Rossi *et al.*, 2013a]. The significant offshore mass transport along the major axis of a filament is larger than that possible by purely wind-driven Ekman dynamics [Relvas *et al.*, 2007]. Calculations by Rossi *et al.*, [2013a] have suggested that filaments are responsible for greater offshore transport of coastal properties in the Iberian system (~60% of total cross-shelf exchanges) and carbon export by filaments is 2.5–4.5 times that due to Ekman transport [Álvarez-Salgado *et al.*, 2007]. Overall, filaments provide an important mechanism for exchange of materials between coastal and offshore waters, especially the transport of chlorophyll [Rossi *et al.*, 2013a], nutrients [Cravo *et al.*, 2010], and carbon [Santana-Falcón *et al.*, 2016].

In situ observations in Western Iberia have elucidated some aspects of the physical and biological oceanography of upwelling filaments. The offshore flow was found to be limited to a relatively thin surface layer, with the strongest flow observed at the boundaries of the structure, while substantial reverse onshore flow may occur beneath the filament [Barton *et al.*, 2001; Rossi *et al.*, 2013a]. Weak mixing in the core of filaments but enhanced at their boundaries has been reported [Barton *et al.*, 2001]. Note that close to barriers there are strong gradients of transported substances, so that mixing is enhanced in their vicinity. Water within filaments has been found to be relatively homogeneous but well isolated from the surroundings [Rossi *et al.*, 2013a]. Mesoscale eddies near the upwelling front, resulting from the interactions of the poleward subsurface flow with the surface upwelling jet and the topography, seem to contribute to the filament development [Peliz *et al.*, 2002]. Indeed, on some occasions, opposite rotating eddies are observed at the base and the tip of the filament, creating typical mushroom-like structures and promoting its generation and fast offshore development. Last, the riverine coastal low salinity plume often observed off north-west Iberia [Otero *et al.*, 2010] has been mentioned as a possible input of buoyancy to the filamentary structure, possibly promoting its offshore elongation [Peliz *et al.*, 2002; Rossi *et al.*, 2013a]. A complete description of the filaments' characteristics and a better understanding of their dynamics is required to properly assess their role in cross-shelf exchanges.

In this paper, we use Lagrangian tools to study the three-dimensional structure of a coastal cold water filament in a regional simulation of the western Iberian shelf (and adjacent ocean) using realistic forcings. This simulation is coincident with an in situ campaign that studied the biophysical oceanography of the region under upwelling-favorable conditions [Rossi *et al.*, 2010, 2013a]. Hence, our numerical analysis deepens, complements and generalizes that observational study, while, conversely, some aspects of the numerical results are validated by the in situ results of Rossi *et al.* [2013a]. In particular they documented peaks of biological activity associated with the successive upwelling pulses and reported that the offshore transport of enriched, recently upwelled waters, is more efficient through the filament than across the front. The precise reasons behind such an efficient transport within this apparently coherent filamentary structure remained puzzling and motivated the present paper.

We compute 3-D fields of finite-size Lyapunov exponents (FSLE) and extract the 3-D boundaries of the filament as ridges of the FSLE fields. Virtual particles are released and tracked numerically in order to characterize the dynamics of the water masses inside the filament. Section 2 describes the data and methods used in this work, while section 3 presents and discusses the results. Section 4 discusses the results and conclusions are drawn in section 5.

## 2. Data and Methods

### 2.1. Area and Period of Study

To allow validating and complementing our numerical approach with observations, we focus on the central region of the Iberian upwelling in late summer 2007. This is concomitant with the MOUTON07 survey which studied the physical and biogeochemical variability of the coastal upwelling and of its connection with the open ocean.

More details about the MOUTON07 campaign and data set are reported in the literature. In particular, Rossi *et al.* [2010] observed a secondary "shelf-break" upwelling front, in addition to the common coastal one, and proposed a physical mechanism for its generation with the use of numerical modeling. Rossi *et al.* [2013a] investigated the cross-shore variability and transport in the central Iberian upwelling by comparing two zonal sections across the front and an extensive sampling of an upwelling filament originating at about 40.3°N and developing through September.

We thus focus our numerical analysis on the central Iberian upwelling in September 2007. This period still falls within the upwelling season but it experienced low to moderate northerly winds, hence favoring the formation and maintenance of well-defined filaments.

### 2.2. Simulations of the Iberian Upwelling

The oceanic simulations were done using the Regional Ocean Modeling System (ROMS) [Shchepetkin and McWilliams, 2005]. ROMS is a free-surface terrain-following model which solves the primitive equations using the Boussinesq and hydrostatic approximations. This state-of-the-art model is highly configurable for realistic applications and has been applied to a wide variety of space and time scales across the world [Haidvogel et al., 2008].

The model domain covers the Portuguese and Galician region, extending well beyond the shelf break (13.25°W to 7.5°W and 35.6°N to 45°N) with horizontal resolution of 2 km in the meridional direction and 1 km in the zonal direction (see Figure 1). The vertical discretization used 30  $\sigma$ -layers, stretched to increase resolution near the surface and bottom. The bathymetry is interpolated from ETOPO and smoothed to satisfy a topographic stiffness-ratio of 0.2 [Haidvogel and Beckmann, 1999]. The minimum depth used is 3 m. The configuration uses a fourth-order horizontal advection scheme for tracers, a third-order upwind advection scheme for momentum, and the turbulence closure scheme for vertical mixing by Mellor and Yamada [1974].

The simulations were initiated from November 2003 and ran until the end of 2007 with realistic initial and boundary conditions from the global model HYCOM, thus providing daily outputs over years 2003–2007, overlapping with the timing of the field survey. HYCOM [Wallcraft et al., 2009] has horizontal resolution of 1/12° and the data is available at 33 vertical layers. This model assimilates observations from several sources including satellite altimetry, satellite, and in situ temperatures, and vertical temperature and salinity profiles from XBTs and ARGO buoys. The offline nesting procedure employed here used a nudging region of 40 km along the model boundaries. In this layer, the 3-D model variables (temperature, salinity, and currents) were pushed toward HYCOM outputs with a time scale of 8 h. The nudging was set to a maximum at the boundaries, decaying sinusoidally to zero inside the nudging layer. At the boundaries, radiation conditions were used for the baroclinic variables [Marchesiello et al., 2001]. Sea surface height and barotropic currents from the parent models were imposed at the boundaries following Chapman [1985] and Flather [1976]. Tidal forcing was employed at the lateral boundaries, as amplitudes and phases of tidal elevation and as barotropic tidal ellipses of the main diurnal and semidiurnal tidal constituents. This forcing was obtained from the 1/12° Atlantic data set of TPXO [Egbert and Erofeeva, 2002].

ROMS has been applied in many coastal modeling studies in the region such as studies of dispersion and recruitment of larvae [Marta-Almeida et al., 2008], river plumes [Otero et al., 2008], and pollution transport

[Marta-Almeida et al., 2013a]. While these studies were based on climatological open boundary conditions, offline nesting has been adopted in the current work to improve realism. It has been shown that using an assimilating parent model improves the ROMS skill [Hetland, 2006], even when parent and child are forced with different atmospheric data [Marta-Almeida et al., 2013b]. Other works have used the same nesting procedure and HYCOM as parent model [e.g., Barth et al., 2008; Zhang et al., 2012; Fennel et al., 2013; Amorim et al., 2013].

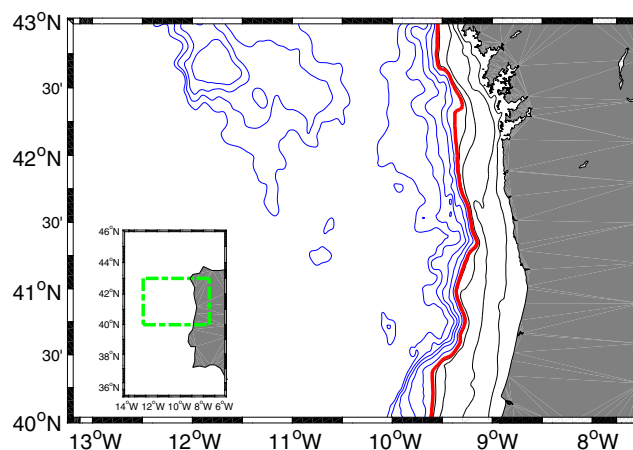


**Figure 1.** Region of calculation of the 3-D FSLE fields. Thick red line: 250 m isobath; Black lines: 50, 100, 150, 200, and 250 m isobaths; Blue lines: isobaths between 500 and 2500 m, drawn every 500 m. Inset: ROMS hindcast region and FSLE region (green rectangle).

Surface heat and freshwater fluxes from ERA-INTERIM [Dee et al., 2011] were used, with a resolution of 0.75°. As wind forcing, data from the Cross-

Calibrated Multi-Platform (CCMP) Ocean Surface Wind Vector Analyses [Atlas *et al.*, 2010] were used. CCMP uses a variational analysis method to combine data from satellite sources, producing 0.25° gridded winds every 6 h.

River discharges from the main Portuguese and Spanish rivers were obtained from the national institutes and were included here by using the procedures described by Otero *et al.* [2010]. Flow data of large rivers (e.g., Douro and Minho) come from measurements obtained during the period of study while others are monthly climatologies (due to absence of data). River temperatures were set equal to the local climatological air temperatures [da Silva *et al.*, 1994].

### 2.3. Lagrangian Coherent Structures and Finite-Size Lyapunov Exponents

We characterize the filamental structure based on the computation of Lagrangian Coherent Structures (LCS). These are structures that separate different dynamical regions of the flow, serving as proxies for barriers and avenues to transport or eddy boundaries [Boffetta *et al.*, 2001; Haller and Yuan, 2000; d'Ovidio *et al.*, 2004]. We are interested in a fully 3-D characterization of the LCS that delimit the frontiers of the filament. For this we follow work done in Bettencourt *et al.* [2012] in another upwelling region (Benguela) to unveil the dynamics of a mesoscale eddy moving offshore. Thus the LCS are computed as the ridges with high values of the FSLE fields [d'Ovidio *et al.*, 2004, 2009; Bettencourt *et al.*, 2012, 2013]. It is important to mention that the particle trajectories are integrated backwards-in-time so that we compute the so-called attracting LCS. These are the most relevant for their physical implications since particles typically approach and spread along them [d'Ovidio *et al.*, 2004; Bettencourt *et al.*, 2012]. LCS are tolerant to imprecisions in the velocity field [Hernandez-Carrasco *et al.*, 2011]. The time scales for all the biophysical processes that we study (for example, a significant variation of the position of the eddies) are much larger than one day, which makes it acceptable to use daily model outputs.

The FSLEs,  $\lambda$ , measure particle dispersion at finite scales and were introduced to study nonasymptotic dispersion processes such as stretching at finite scales and bounded domains [Artale *et al.*, 1997; Aurell *et al.*, 1997; Boffetta *et al.*, 2001]. They are defined as:

$$\lambda(d_0, d_f; \mathbf{x}_0, t) = \frac{1}{\tau} \log \frac{d_f}{d_0}, \quad (1)$$

where  $\tau$  is the time it takes for the separation between two particles, initially  $d_0$ , to reach a value  $d_f$ . In addition to the dependence on the values of  $d_0$  and  $d_f$ ,  $\lambda$  depends also on the initial position of the particle  $\mathbf{x}_0$  and the time of deployment  $t$ .

The  $\lambda$  fields in the region of interest (Figure 1) were computed following the method of Bettencourt *et al.* [2012], using  $d_0$  equivalent to one half of the horizontal spacing of the ROMS grid. In brief, the FSLE is computed in a 3-D grid of initial conditions, composed of constant depth layers, in a quasi-3-D fashion: the particle trajectories are computed using the 3-D velocity field but the calculation of the interparticle distance only considers horizontal distances. In addition, the ridges delimiting the filament are computed in 3-D space, following the methodology outlined in Bettencourt *et al.* [2012]. To do this, the  $\lambda$  field was smoothed [Garcia, 2010] and high-pass filtered to remove the small-scale noise. The smoothing process has the side-effect of smearing the FSLE gradients, which reduces the ridge strength and makes it harder for the extraction algorithm to delineate the complete filament boundaries.

The vertical resolution of the FSLE computation is variable with 30 horizontal levels between 5 and 200 m depth, clustered near the surface. The final distance threshold  $d_f$  was set at 100 km and the particles were integrated for 90 days with a fourth-order Runge-Kutta method, using the ROMS velocity fields from June to December 2007. We note that with a 90 day integration period the smallest  $\lambda$  that can be measured is  $0.05 \text{ d}^{-1}$ , but for plotting purposes, we assign a value  $\lambda = 0$  to the initial conditions for which the final separation  $d_f$  is not reached after the 90 days integration period. FSLE fields were computed daily from late August to early October when filament activity is stronger [Haynes *et al.*, 1993].

Offshore transport through the filament was further investigated by computing particle trajectories released at the filament root. Particles were released at 9°30'W on 26 September 2007 at 7, 12, 24, 29, and 34 m depth. At each depth, seven particles were released along a line between 41°30'N and 41°35'N, inside the filament root. Particle trajectories were integrated until the year's end (i.e., during about 3 months). Only

the particles that travelled offshore of 10°30'W were considered in the analysis. Temperature and salinity fields were interpolated along the particle trajectories [Chenillat et al., 2015].

### 3. Results and Discussion

#### 3.1. Oceanographic Background and Mesoscale Structures From FSLE Fields

The dynamics in the region is dominated by a complex pattern of mesoscale and submesoscale features at different depths as shown in Figure 2. Lines of high  $\lambda$  are found mainly on the boundaries of the dominant mesoscale structures. The surface field is markedly noisy, while the deeper levels show less small-scale features. The coastal strip, of about 20–50 km width (up to around 9°30'W), is characterized by weak  $\lambda$  and patches where  $\lambda < 0.05 \text{ d}^{-1}$ , identifying zones of weak dispersion of fluid elements.

On 26 September 2007, the dominant structure is a large anticyclonic eddy with center located at 42°N/10°30'W and a diameter of  $\sim 100 \text{ km}$  (labeled AC in Figures 2a and 3). Westward of this warm-core eddy, a cyclonic eddy (centered at 42°15'N/11°45'W) is found, labeled CC1 in Figure 2a which, together with the former eddy, assemble a mushroom-like dipole structure. Between them, an elongated high-strain region can be found, signaled by the concentration of parallel high  $\lambda$  lines. The dipole is pulling fluid from the south along its meridional axis. South of the latter cyclonic eddy we find an additional anticyclonic eddy (centered at about 40°15'N/12°30'W), labeled AC1 in Figure 2a forming another dipolar structure with the CC1 eddy, a situation previously observed [Fedorov and Ginsburg, 1989]. This second dipole has an axis orientated along the zonal direction and is pulling fluid toward the shelf. The fluid advected zonally by this second dipole is slightly colder (see Figure 3c) than the water within the core of the AC1 eddy. It thus appears as a colder water tongue along the dipole axis, that is deflected southward due to the AC1/CC eddies.

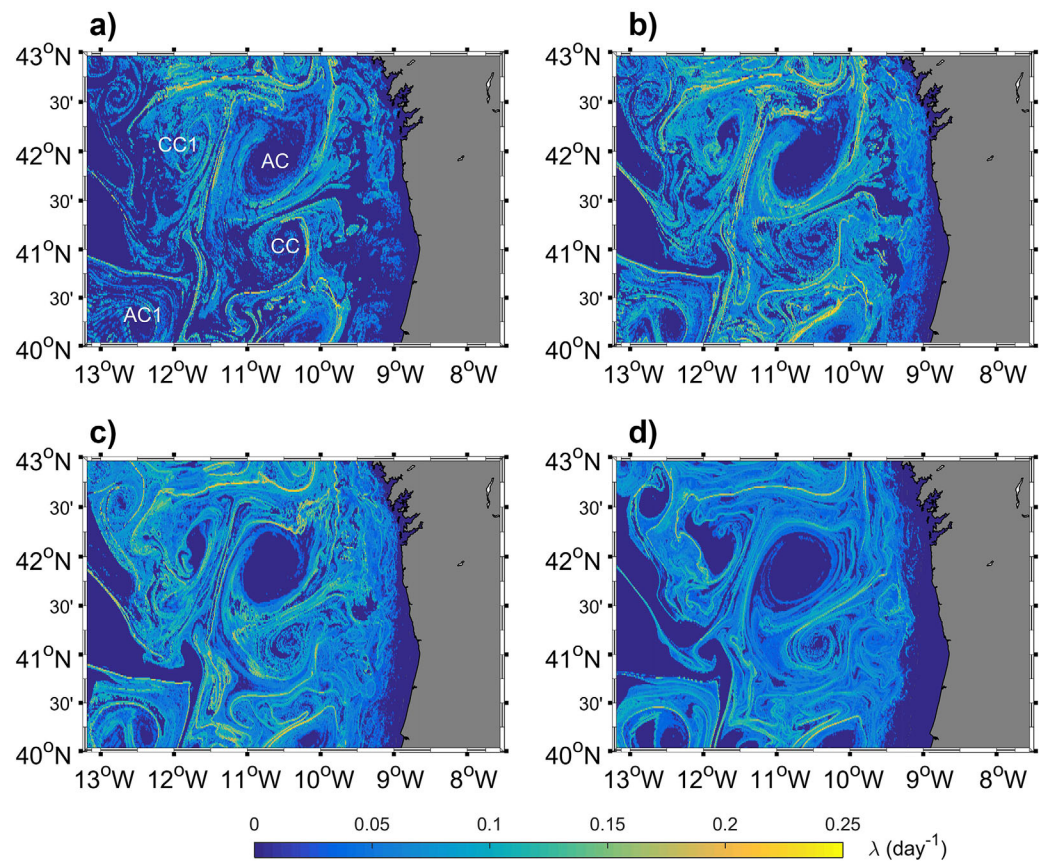


**Figure 2.** Backward FSLE field on 26 September 2007. (a) 9.8 m depth; (b) 17.1 m depth; (c) 31.8 m depth; and (d) 96.8 m depth. For the labels in Figure 2a, see text in section 3.1.

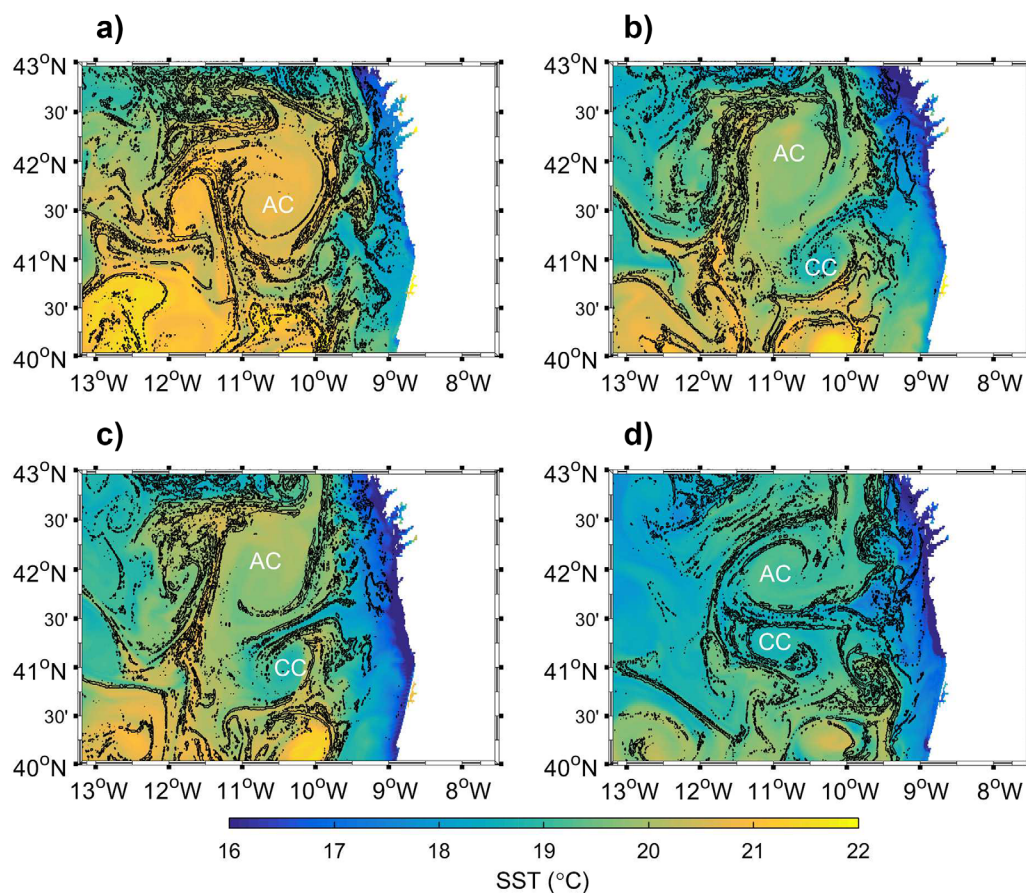


**Figure 3.** Filament evolution. (a) SST and backward FSLE contours ( $0.1 \text{ d}^{-1}$ ) on (a) 9 September 2007; (b) 20 September 2007; (c) 24 September 2007; and (d) 6 October 2007. For the labels see text in section 3.1.

Concerning the coastal patches of small  $\lambda$ , the one centered on  $41^{\circ}30'N/9^{\circ}30'W$  at 9.8 m depth (Figure 2a) has a thin south-westward extension that provides an offshore transport pathway for coastal waters in-between the AC and CC eddies. This is the filamentary structure that will be thoroughly studied in the rest of the paper. The weak dispersion evidenced by  $\lambda < 0.05 \text{ d}^{-1}$  indicates that the fluid particles released from this region will evolve, backward in time, along nearby trajectories with very small divergence between particle pairs. In other words, nearby particles passing through these regions come from nearby initial positions. Observing the deeper levels in Figure 2, we can see that the  $\lambda < 0.05 \text{ d}^{-1}$  patch is present at 17 m depth (Figure 2b) and at 32 m depth (Figure 2c), becoming smaller with depth. This could indicate the presence of an upwelling cell, i.e., a region through which subsurface fluid parcels rise to the surface and subsequently drift offshore, as shown in section 3.2.

There are other regions where  $\lambda$  is small. The AC eddy shows  $\lambda < 0.05 \text{ d}^{-1}$  in its core at all depths shown in Figure 2. Note however that the AC eddy is not completely enclosed by high  $\lambda$  lines since it presents openings with  $\lambda \neq 0$  at its north-east and south-west sectors (e.g., Figure 2b). High  $\lambda$  lines symbolize “coherent” boundaries that clearly separate waters in the AC core from the surrounding waters. In contrast, areas with small  $\lambda$ , bounded by parallel high FSLE lines, represent preferential avenues of transport for water to enter and exit the AC eddy. They also indicate the likely pathways of transport: water of northern origins enter the AC through the north-east open boundary; coastal waters that were previously advected offshore through the filament (in between AC and CC) then tend to recirculate into AC via the south-west open frontier. These pathways are imposed by the anticyclonic circulation and have been confirmed by particle trajectories analysis.

### 3.2. Formation and Evolution of the Coastal Filament

The rest of the paper will be devoted to the detailed study of the filamentary structure identified in the previous section flowing (south)westward between eddies AC and CC. It was formed during the second half of

September 2007 and was perfectly noticeable on September 20 (Figures 3b and 3c) as a cold water tongue connecting the coastal recently upwelled water with a cyclonic recirculation centered around 41°N and 10°30'W, labeled CC in Figures 3b, 3c, and 3d.

The physical mechanism for the formation of the filament is beyond the scope of this paper; however, we will in this section provide a short description of its formation. The cold water filament started as a coastal cold water pool that is entrained toward warmer waters offshore of the upwelling front. This pool is centered at 41°15'N and 9°30'W on 9 September (Figure 3a). Adjacent to this cold water intrusion, the cyclonic recirculation still in an initial stage is located slightly to the south-west.

The filament formation could result from the interaction between the anticyclonic eddy AC and the coastal topography. Indeed, several observational and numerical studies documented the association of mushroom-like dipolar structure with the thin filaments favoring cross-shore water transport [Churchill *et al.*, 1986; Oey and Zhang, 2004; Sutyryn and Grimshaw, 2010; Meunier *et al.*, 2010; Rossi *et al.*, 2013a]. In particular, Sutyryn and Grimshaw [2010] and Meunier *et al.* [2010] used numerical simulations to study how along-shore currents interact with the shelf bathymetry to create topographic eddies. They showed that an anticyclonic eddy first develops upstream and it is closely followed by the formation of a cyclonic secondary circulation downstream. Fed by shelf waters with high potential vorticity, both anticyclonic and cyclonic vortices interact as a dipolar structure which forms an elongated, trapped, and narrow filament along its axis.

The dynamics of the filament seem tightly linked to the evolution of both anticyclonic (AC) and cyclonic (CC) eddies forming the dipole. On 20 September, the CC eddy has grown and the potential temperature (henceforth temperature) is lower than the surrounding waters due to the injection of recently upwelled waters within the cold water filament. Four days later (Figure 3c), the filament axis is mainly zonal and its southern seam continues exporting colder water offshore.

Remarkably, there is a parallel offshore motion of warmer waters in the northern flank of the cold water filament. The northern warm water channel, influenced by the adjacent AC eddy, pulls water of about  $\theta \simeq 19\text{--}20^\circ\text{C}$  that is isolated from the recently upwelled waters due to a series of transport barriers (signaled by the high FSLE lines along the contact zone between the eddy and the upwelling front, Figures 2a and 2b). The cold water filament starts on the shoreward side of the upwelling front, thus pulling colder water of about  $\theta \simeq 17\text{--}19^\circ\text{C}$  offshore (Figure 3c).

The filament continues developing. On 6 October (Figure 3d), the mushroom-like dipole formed by the CC and AC eddies (now exhibiting almost similar diameters of 80 km) is well developed and drifts offshore. It results in an extension of the filament length which continues transporting colder water offshore. Note that the temperature differences between the filament core and its surroundings have diminished as compared to 2 weeks before which could be related to a new upwelling pulse and/or to some air-sea processes (such as solar warming or wind-induced cooling) have diminished relatively to the previous weeks as expected due to the onset of Autumn conditions (lower solar radiation and northern wind associated with colder air temperature). The filament continues to evolve further but its signature on SST is significantly reduced.

On 24 September 2007, which is the date where the FSLE fields most clearly represent its structure (Figure 3c), the filament under study is about 140 km long and 10 km wide. The northern warmer channel has a width of 15 km. At its maximum extension, the filament is about 230 km long. Those dimensions are consistent with observations [e.g., Rossi *et al.*, 2013a, and references therein].

### 3.3. Vertical Properties of the Filament

The filament appears as a thin elongated region of  $\lambda < 0.05\text{ d}^{-1}$  at 9.8 and 17.1 m depth (Figures 2a and 2b). The signature is absent on deeper levels, indicating the shallow nature of this corridor transporting shelf water to the offshore. A vertical section through the backward  $\lambda$  field on 26 September 2007 (Figure 4) shows its vertical extent to be about 30 m deep, in good agreement with previous observations-based estimates [Rossi *et al.*, 2013a].

At the northern border of the filament, there is a shallow strip that constitutes the northern channel through which relatively warmer waters recirculate. The boundaries of the AC eddy intersect the plane northward of the filament, indicating that the surface section of the eddy is slanted toward the north with respect to the deeper levels, especially its northern flank, also characterized by the highest  $\lambda$ . The CC eddy is seen south of the filament, presenting higher values of  $\lambda$  in its core, centered at 41°N. A possible reason

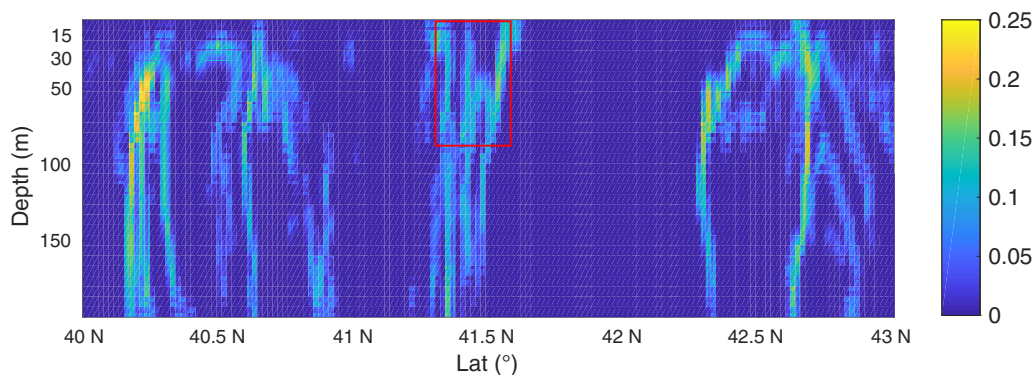


**Figure 4.** Vertical section of backward FSLE taken at  $10^{\circ}15'$  W on 26 September 2007. The FSLE field was smoothed and filtered to improve clarity and highlight the main features of the FSLE field. The filament area is highlighted in the red rectangle.

for the difference in the  $\lambda$  field inside both eddies is that, because the CC eddy is young compared to the AC eddy, the backward  $\lambda$  field in its interior reflects the different origins of the waters that formed the eddy, while the waters in the older AC eddy have been isolated from the exterior for more than 90 days (the FSLE integration time).

### 3.3.1. Thermohaline Vertical Structure

$\lambda$ ,  $\theta$ , and salinity fields were interpolated linearly along a selected section within the filament (white line on Figure 5) on 26 September. The cross-shore and vertical variations of these quantities are shown in Figure 6. The filament appears as a shallow feature in the  $\lambda$  field (Figure 6a) with central portions not deeper than 25 m. At the root, approximately 40 km from the coast, the filament is deeper than 50 m but its size diminishes with increasing depth. This can also be observed in Figure 2, where the size of the  $\lambda < 0.05 \text{ d}^{-1}$  area at the root of the filament decreases with depth. Offshore, the filament becomes shallower until it vanishes within open ocean waters at  $\sim 200$  km offshore. We can observe that before reaching the offshore tip of the filament, the  $\lambda < 0.05 \text{ d}^{-1}$  region has curved southward to join the CC eddy that is receiving the water exported through the filament. The temperature profile (Figure 6b) indicates that the filament is composed of recently upwelled water ( $\theta \leq 17^{\circ}\text{C}$ ) at the shoreward tip that progressively warms up as it flows through the filament. There is a noticeable vertical  $\theta$  gradient located at about 30–60 m below the surface. The salinity profile (Figure 6c) shows a pool of freshwater located at the root of the filament down to 30 m. This type of low salinity lens is commonly observed in the region [Otero *et al.*, 2008, 2010; Rossi *et al.*, 2013a] but it is still unclear if it originates from continental freshwater inputs and/or from recently upwelled waters (such as the low salinity Eastern North Atlantic Central Waters). The salinity then gradually increases westward until reaching a maximum 140 km offshore from the filament root. The thermohaline structure of this simulated filament appears to be in very good agreement with the observations of Rossi *et al.* [2013a]. In particular, both vertical and horizontal structures as well as gradients are very similar when comparing our Figures 6b and 6c and Figures 7b and 7c of Rossi *et al.* [2013a].

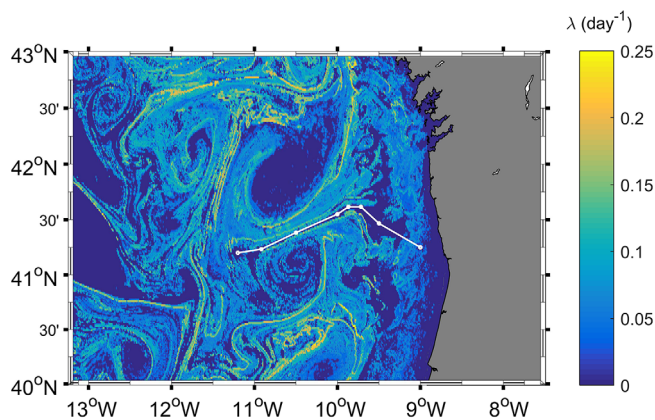


**Figure 5.** Location of the profile path (white line) taken along the filament on the 26 September 2007. FSLE map at 14.7 m depth.

Note that between 140 and 180 km from the coast, there is a clear uplifting of isotherms, also noticeable as a doming in the  $\lambda$  field (Figure 6a), caused by the cyclonic eddy situated to the south of the profile. This is a typical situation where small structures superimpose their signatures on top of the larger (mesoscale) filament [Rossi *et al.*, 2013b].

### 3.3.2. Particle Trajectories Within the Filament

Tight clusters of five particles were released from five initial depths (Figure 7)

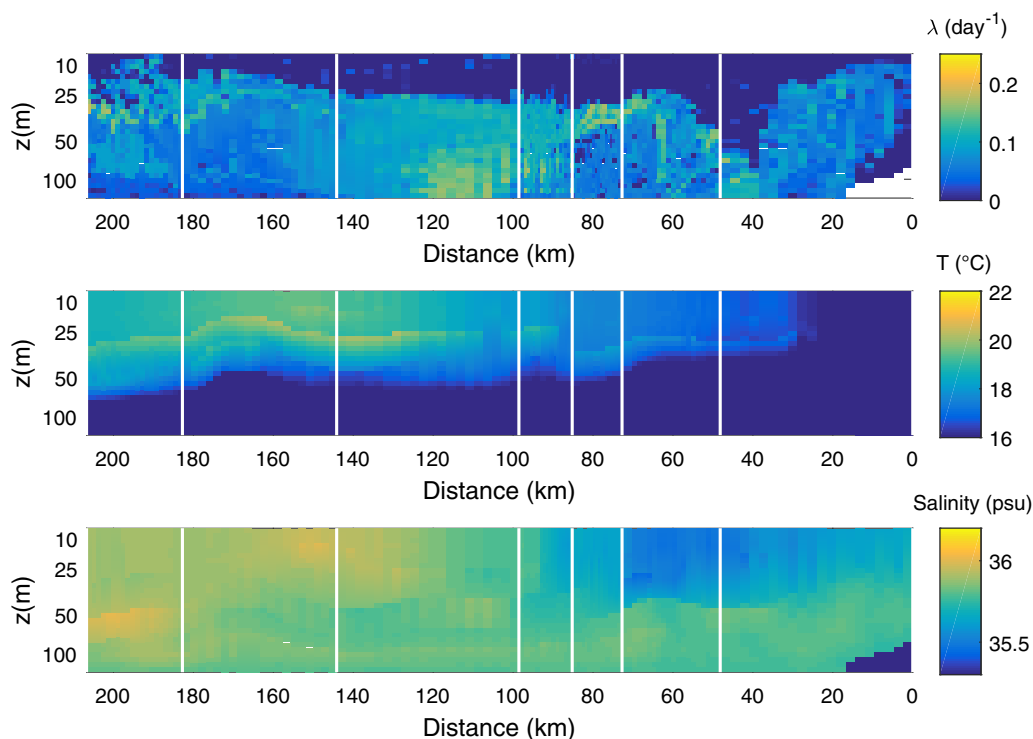


**Figure 6.** Profiles along filament on 26 September 2007. (a) Backward FSLE; (b) Temperature; and (c) Salinity. White vertical lines represent locations of profile of the white circles marked along the profile (white line of Figure 5). Fields were interpolated linearly at 20 equally spaced points in between nodes. Distance along profile increases toward the offshore.

to illustrate the dynamics of the trajectories starting at the root of the filament. The horizontal particle trajectories (Figure 7a) clearly separate the set in two groups depending on the release depth: shallower released (7 and 12 m) particles flow through the filament and then into the cyclonic circulation while deeper released particles turn northward into the anticyclonic eddy when they exit the filament. That the release depth is the factor determining the fate of the particles should not be a surprise since the filament boundaries are slanted in the vertical and deeper particles will be on one side of the boundary while shallower particles will be on the other side. Note some exceptions occur such as some particles released at 7 m that follow the filament but end-up circulating around the anticyclonic eddy or the particle released at 34 m that travels northward before entering the anticyclone.

The maximum zonal displacement is  $\sim 200$  km (Figure 7b). The shallow particles that flow through the filament experience a subduction and reach their deepest positions  $\sim 60$  km after release. They then begin to rise briefly until the 100 km offshore mark. The “red” particles enter the cyclonic circulation and sink, while the “green” particles remain approximately at the same depth. The two red particles that enter the anticyclonic circulation eventually rise when their trajectories curve to the north. The different behavior of the “green” and “red” particles is most likely caused by the fact that red particles, circulating further from the cyclone’s center, tend to follow deeper isotherms than the green particles.

The temperature-salinity ( $\theta$ -S) diagram (Figure 8) associated with these particles reveals that their initial properties (at the release depth) are quite similar in terms of salinity but distinct in terms of  $\theta$ , with variations as much as  $1^\circ\text{C}$  (crosses on Figure 8). The coldest water is found at 24 m depth and the warmest at 29 m depth, warmer than the shallow release locations. This is caused by the location of the sharp  $\theta$  gradient at the bottom of the mixed layer in the filament root. The temperature profile (Figure 6b) shows that this gradient coincides with the two deeper sets of particles and that these subsurface waters can be slightly warmer than surface layers. The two shallower sets (red and green particles) then essentially evolve along pathways during which their density is conserved (Figure 8), representing transport along isopycnals. The remaining sets (blue, magenta, and black) show contrasting evolutions with important changes of their

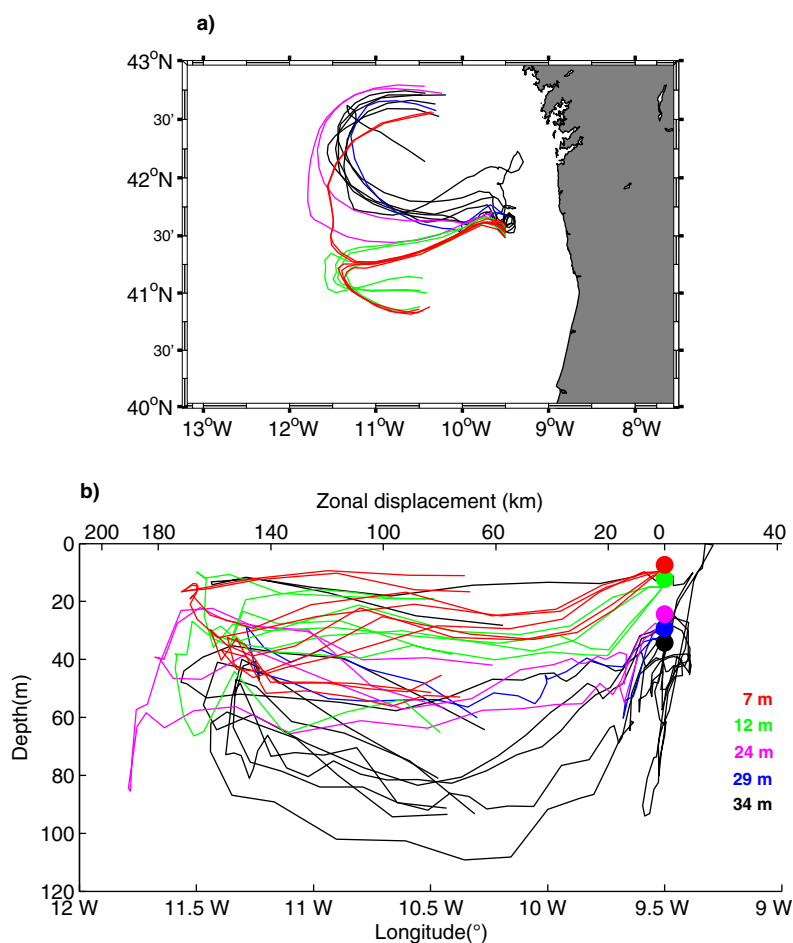


**Figure 7.** Trajectories of particles released at the root of the filament. (a) Horizontal projection of the trajectories; (b) Vertical and longitudinal displacement along the particles trajectories. Particles were released at  $9^{\circ}30' \text{ W}$  at 26 September 2007 at 7, 12, 24, 29, and 34 m depth and were integrated until year's end. Only the particles that traveled offshore of  $10^{\circ}30' \text{ W}$  are shown, until they crossed the same longitude in the opposite direction.

temperatures, suggesting the presence of diapycnal mixing (i.e., transport of water parcels across isopycnals, resulting in changing thermohaline properties).

### 3.3.3. Horizontal Gradients of Temperature in the Filament

Next, we analyze the norm of the horizontal gradient of temperature on 26 September 2007 at 12.25 m depth together with contours of  $\lambda$  (Figure 9). The filament boundaries appear both as high  $\lambda$  regions and as strong temperature gradient norm. This coincidence is verified in several other regions of the domain, but not exactly everywhere.

We note specially the strong  $\theta$  gradients along  $\sim 9.5^{\circ} \text{ W}$  that signal the shelf break front separating cold recently upwelled water masses from warmer offshore waters. This is not a continuous feature but it presents instead a complex wave-like aspect with the dominance of submesoscale patterns. It suggests that vertical dynamics becomes more important closer to the coast. This could explain the poor matching between  $\lambda$  maxima and strong  $\theta$  gradient features in the shelf region since the  $\lambda$  computation was tuned to mesoscale features.

On the other hand, the filament boundaries are properly captured by the  $\lambda$  and by the  $\theta$  gradient fields. The root of the filament appears to the southern end of a cold water region situated inshore of the frontal features between  $41.30^{\circ} \text{ N}$  and  $42.30^{\circ} \text{ N}$ . Capturing the filament boundaries using both methods returned good agreement probably because the dynamics giving rise to the filament, the pair of counterrotating eddies, occurs at the mesoscale and off the shelf. Also, the fact that particles flowing through the filament conserve their (potential) density (section 3.3.2) further supports the finding of matching  $\lambda$  maxima and strong

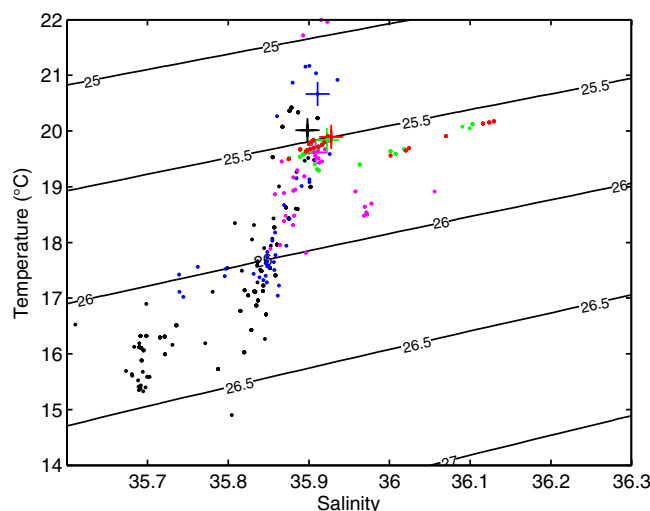


**Figure 8.** Temperature-Salinity ( $\theta$ - $S$ ) diagram of particles released at the root of the filament. Black lines in the diagram are constant density lines in  $\text{kg}/\text{m}^3$ . Crosses indicate the  $\theta$ - $S$  properties at the release location.

horizontal gradient norms. Moreover, through a careful examination of Figure 9, it is evident that  $\lambda$  maxima match strong  $\theta$  gradient features along the boundaries of most mesoscale eddies and filamentary structures.

### 3.4. 3-D Structure of the Filament

The 3-D Lagrangian structure of the filament is investigated by extracting ridges in the 3-D backward  $\lambda$  field. These ridges approximately coincide with attracting Lagrangian Coherent Structures (LCS) of the flow [d'Ovidio *et al.*, 2004; Mancho *et al.*, 2006; Prants, 2013; Haller, 2015]. To avoid unnecessary computational effort, the ridge extraction was limited to a subregion that contains the filament, i.e., between  $11^{\circ}20'W$  and  $9^{\circ}30'W$ ,  $41^{\circ}N$  and  $41^{\circ}45'N$  and over 7–70 m (see Figure 1).

The relevant ridges on 26 September 2007, that best reveal the Lagrangian dynamics of the filament, are shown in Figure 10. They are the boundary of the anticyclone (in green), the boundary of the cyclone (in blue), and the LCS that separates the cold water filament from the northern warm water channel (in red). Levels of the  $\lambda$  field are plotted together with the 3-D ridges at 20 m depth (Figure 10a) and at 45 m (Figure 10b). As discussed by Bettencourt *et al.* [2012], the ridges fall on the high  $\lambda$  lines which give confidence to our 3-D computation. Fluid elements flow along attracting ridges of the FSLE field, so the blue ridge is moving fluid offshore from the filament root. The green ridge, on the other hand is separating the fluid inside the anticyclone from the water that is outside but flows around it. Note that, at least at the surface, this water mass is warmer than in the filament core (Figure 3c) so there should be a barrier separating these two streams and preventing them from mixing. On the  $\lambda$  map at 20 m depth (Figure 10a), there is a line of high  $\lambda$  separating these regions (white lines), but the automatic extraction process found no ridge there. In contrast, it found a ridge separating both streams at 45 m (Figure 10b). It is possible that the ridge extraction threshold was set higher than the intensity of this high FSLE line or that the smoothing of the FSLE field reduced artificially the ridge strength, thereby rendering it invisible to the extraction algorithm. However, the purpose of this analysis is the delineation of the filamentary structure, so that the threshold was set accordingly after preliminary tests (not shown). The retained threshold is a compromise between a value small enough to extract the relevant boundaries but big enough not to capture the many smaller-scale less energetic structures.

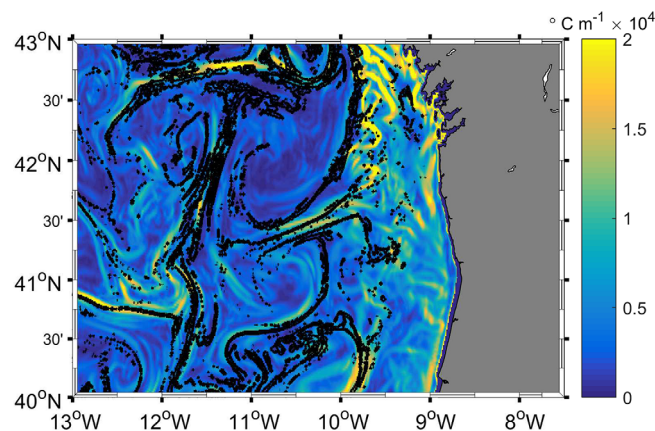


**Figure 9.** Map of the norm of the horizontal temperature gradient at 12.25 m depth, together with contours (black lines) of backward FSLE at the  $0.12 \text{ d}^{-1}$  level on 26 September 2007.

The 3-D shapes of the LCSs delimiting the filament, and their relationship with the thermohaline structure, are clearly depicted in Figure 11 from another perspective (looking along the filament axis towards offshore). The 3-D LCSs are located around and at the transition between both mesoscale structures. The LCS which separates both eddies and also the cold and warm water offshore flows (red)

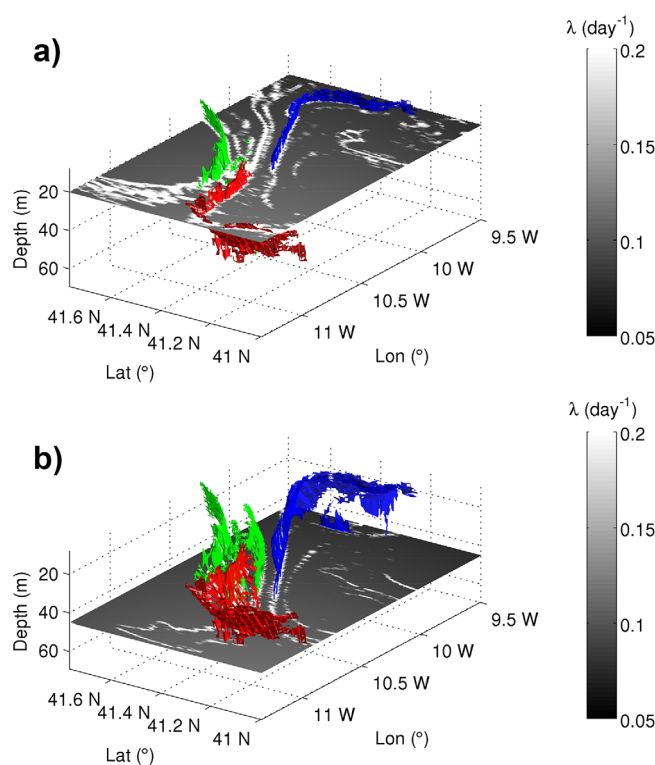


**Figure 10.** Two views of the ridges of the 3-D FSLE field defining the filament extracted on 26 September 2007. Green: boundary of the anticyclone; Blue: boundary of the cyclone; Red: Ridge that separates the cold water filament from the northern warm water channel. (a) FSLE field at 20 m depth; (b) FSLE field at 45 m depth.

is connected to the anticyclonic LCS (green, see Figure 10). Although a discontinuity is visible (related to the ridge extraction process), the green LCS constitutes a coherent curtain in the vertical separating clearly the filament from the adjacent anticyclonic eddy. The cyclonic curtain-like LCS (blue) also reveals continuity in the vertical except at the root of the filament (interrupted between 30 and 40 m depth). Note also that the size of the cyclonic LCS (blue) in the filament root diminishes with depth, confirming the contraction of the filament root (source region) already documented in Figure 2.

As suggested by previous analysis in section 3.3.3, the thermohaline structure of the filament is related to these dynamical barriers. The main temperature and salinity fronts match the curtain-like 3-D LCSs. There are clear temperature differences between surface and subthermocline waters, as well as between the cyclone, where isotherms are raised, and the anticyclone, where they are depressed (Figure 11). The cyclone LCS is positioned

between the CC eddy and the filament, although it does not coincide exactly with the boundary of the cold water due to the warm tongue of water that is being pulled by the CC eddy and visible in Figure 3c. In accord with previous interpretation, the salinity structure (Figure 11b) reveals the distinct origins of the anticyclonic and cyclonic branches of the filament: the former has warm, saltier water while the latter has colder and fresher waters entering the filament from nearshore regions.

#### 4. Discussion

Coastal/offshore exchanges are the product of mainly two mechanisms: a linear response to alongshore wind stress in the form of coastal upwelling and nonlinear dynamics in the form of mesoscale and submesoscale processes. *Combes et al.* [2013] studied the effects of linear (Ekman upwelling) and nonlinear (mesoscale eddies) circulation dynamics on the statistics of advection of coastal waters. They found that the low-frequency cross-shelf transport of the upwelled water mass is strongly correlated with the pulses of alongshore wind stress, but that offshore transport of surface coastal properties is modulated by intrinsic mesoscale eddy activity, in particular cyclonic eddies. Our analyses also revealed that a preferential offshore transport of coastal waters occurred through the shallow filament that fed cyclone CC during its formation. In particular, the particle release experiment described in section 3.3.2 showed that particles released closer to the surface were preferentially captured by the cyclone while particles released from deeper locations were captured by the anticyclone, due to the southward slanting of the filament boundaries. Waters in the filament maintain constant density, suggesting transport along isopycnals, while those below the filament in general cool during their advection offshore, probably due to diapycnal mixing, although some trace out warming waters.

The CC eddy was fed by the water transported through the southern channel of the filament containing the cold coastal upwelled water while the northern channel carried warmer water on the offshore side of the

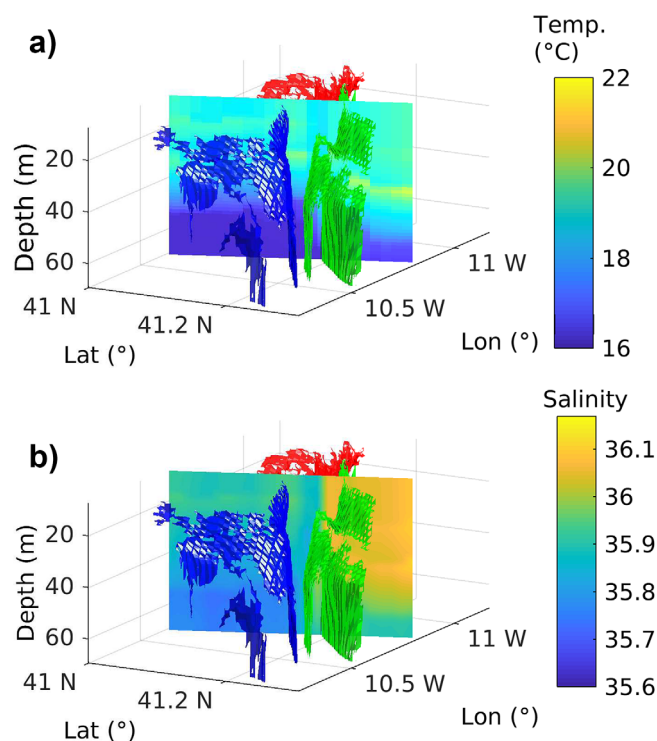


**Figure 11.** Ridges of the 3-D FSLE field defining the filament extracted on 26 September 2007. Green: boundary of the anticyclone; Blue: boundary of the cyclone; Red: Ridge that separates the cold water filament from the northern warm water channel. (a) Temperature. (b) Salinity. Temperature and salinity are shown in a vertical plane normal to the filament axis that passes through 10°27' W. Note opposite perspective relative to Figure 10.

upwelling front in to the AC eddy. This is similar to the work in Nagai *et al.* [2015] that showed that filaments are very effective in transporting coastal material further offshore until they form eddies at their tips which eventually destructure the exporting conduit. Cyclonic eddies tend to trap the cold, nutrient, and organic matter-rich waters of the filaments, whereas the anticyclones formed nearby encapsulate the low nutrient and low organic matter waters around the filament. Here we did not track the filament for a sufficient period of time to reach this destructured state but we consistently observed the least coherent boundaries and the smallest temperature gradients at the latest development stage of our filament.

The high- $\lambda$  lines present in the region allowed us to identify the major barriers and pathways of fluid transport, organized by intense mesoscale activity in the form of mesoscale eddies and submesoscale fronts. The filament itself appears as a thin region of  $\lambda < 0.05 \text{ d}^{-1}$ , indicating that the fluid progresses along the filament, with-

out deformation, toward the offshore. The FSLE and its ridges appear as suitable tools to study mass export as they allow to delimit the main exporting structures, at a resolution higher than the underlying velocity field [Hernandez-Carrasco *et al.*, 2011]. On the other hand, Eulerian quantities such as passive tracers are more readily available from gridded data sets or in situ observations but their ability to describe transport structures depends on whether they are conserved or not, as shown in Figure 9.

From the Lagrangian perspective, cross-shelf export appears to be dominated by meso and submesoscale processes as those identified by the extrema of the  $\lambda$  fields. Nagai *et al.* [2015] showed in the Californian upwelling that the lateral export of material is largely controlled by mesoscale processes, involving filaments and westward propagating eddies. While the analysis presented herein is dedicated to a specific filament and therefore does not allow to draw conclusions in a time mean sense, earlier works using the FSLE [Hernández-Carrasco *et al.*, 2014] showed that mesoscale activity was responsible for 30–50% of organic material export in the Benguela upwelling system and Bettencourt *et al.* [2015] revealed that the stirring of the dissolved  $\text{O}_2$  field by mesoscale Lagrangian structures in the Peruvian upwelling system greatly impacted the oxygen minimum zone there.

For the specific event described in this paper, we were able to define the boundaries of the mesoscale structures that controlled the cross-shelf exchange. The cold water flow was formed between the AC and CC eddies and the filament itself was connected to the latter as is evident in the  $\lambda$  maps of Figures 3 and 5 and in the particle trajectories plot (Figure 7). The physical characteristics of the simulated filament studied from a Lagrangian perspective coincide very well with the ones of the filament observed in Rossi *et al.* [2013a], namely 140 km long, about 10 km wide, and up to 30 m deep. The thermohaline structures of both observed and simulated filaments are also very similar: temperatures smaller or of the order of 17°C together with a low salinity lens near the base of the filament; when water flows westward (offshore export) filament waters exhibit warming up to 19°C and increasing salinity. In both the observed and the modeled filaments, strong gradients in water properties separate the interior from the exterior of the structure.

The filament is limited by the 3-D Lagrangian boundaries of the AC and CC eddies, which provide the necessary barriers to mixing of filament waters with outside ones. An additional barrier exists that separates waters that flow around the AC eddy from those that feed the CC eddy with cold, upwelled waters. Note that the different dynamical regimes, in this case the different fates, of the fluid particles that flow along the filament are reflected in the Lagrangian structures deduced from the FSLE fields. Overall, our analyses revealed that local mesoscale processes control the offshore transport efficiency of the upwelling filament. These factors include the origins (e.g., depth) and properties (e.g., is it formed during upwelling pulse or relaxation?) of the source waters, the presence of mesoscale structures, and their characteristics (e.g., their sizes, ages, and directions of rotation) surrounding the filament as well as the internal dynamics within the filament itself (e.g., isopycnal transport or diapycnal mixing).

A novelty of this work is the attempt to provide a 3-D characterization of this process by computing the 3-D ridges of the backward  $\lambda$  fields. These ridges are proxies to 3-D Lagrangian structures that delineate the full 3-D cross-shelf exchange pathways. The ridges shown are, after extensive testing, those with a best quality/extension trade-off. This trade-off is a consequence of the need to balance the removal of small scale noise by smoothing the FSLE field and the need to avoid artificially reducing the FSLE gradients that are necessary to identify the strongest ridges. The results are not optimal yet and we are working on improvements to the extraction algorithm to reduce the impact of this trade-off.

Although the main focus of this analysis was the horizontal transport, vertical motions also play a role in the physical/biogeochemical interactions. For instance, *Omand et al.* [2015] showed that the downward transport of surface carbon was indeed favored by the subduction of a filamental structure associated with mesoscale eddies.

## 5. General Conclusions

In this work, we investigated the full 3-dimensional structure as well as the cross-shore transport properties of an upwelling filament in the Iberian upwelling from a LCS perspective. Specifically, we showed that the filament can be characterized by its dispersion characteristics (its boundaries are formed by LCSs; low dispersion prevails in its interior). We also demonstrated that these dynamical properties are reflected in the hydrographic properties of the filament (LCSs match large gradients of temperature and salinity) allowing us to discuss the degree of isolation of water within the filament. This work opens new opportunities to detect and fully characterize 3-D filamentary (sub)mesoscale oceanic structures and their impacts on the transport and dispersion of tracers. Nevertheless, studying 3-D transport of fluid and tracers in the ocean still remains a challenge due to the predominance of horizontal stretching over vertical motions and the coexistence of diabatic and adiabatic processes. Further work is needed to continue the development of Lagrangian indicators of 3-D transport and mixing in geophysical flows.

### Acknowledgments

The authors acknowledge support from Ministerio de Economía y Competitividad and Fondo Europeo de Desarrollo Regional through the LAOP project (CTM2015-66407-P, MINECO/FEDER) and through a Juan de la Cierva Incorporación fellowship (IJC1-2014-22343) granted to V.R. J.H.B. acknowledges financial support from the Portuguese FCT (Foundation for Science and Technology) and Fundo Social Europeu (FSE/QREN/POPH) through the predoctoral grant SFRH/BD/63840/2009. Data used in this study can be accessed at <https://doi.org/10.5281/zenodo.802324>.

### References

- Álvarez-Salgado, X. A., J. Aristegui, E. D. Barton, and D. A. Hansell (2007), Contribution of upwelling filaments to offshore carbon export in the subtropical Northeast Atlantic Ocean, *Limnol. Oceanogr.*, *52*(3), 1287–1292.
- Amorim, F., M. Cirano, M. Marta-Almeida, J. Middleton, and E. Campos (2013), The seasonal circulation of the Eastern Brazilian shelf between 10° S and 16° S: A modelling approach, *Cont. Shelf Res.*, *65*, 121–140, doi:10.1016/j.csr.2013.06.008.
- Artale, V., G. Boffetta, A. Celani, M. Cencini, and A. Vulpiani (1997), Dispersion of passive tracers in closed basins: Beyond the diffusion coefficient, *Phys. Fluids*, *9*, 3162–3171.
- Atlas, R., R. N. Hoffman, J. Ardizzone, S. M. Leidner, J. C. Jusem, D. K. Smith, and D. Gombos (2010), A cross-calibrated, multiplatform ocean surface wind velocity product for meteorological and oceanographic applications, *Bull. Am. Meteorol. Soc.*, *92*(2), 157–174, doi:10.1175/2010BAMS2946.1.
- Aurell, E., G. Boffetta, A. Crisanti, G. Paladin, and A. Vulpiani (1997), Predictability in the large: An extension of the concept of Lyapunov exponent, *J. Phys. A Math. Gen.*, *30*(1), 1–26, doi:10.1088/0305-4470.
- Barth, A., A. Alvera-Azcárate, and R. H. Weisberg (2008), Benefit of nesting a regional model into a large-scale ocean model instead of climatology. Application to the West Florida Shelf, *Cont. Shelf Res.*, *28*, 561–573.
- Barton, E. (2001), Canary and Portugal currents, in *Encyclopedia of Ocean Sciences*, edited by J. H. Steele, pp. 380–389, Academic, Oxford, doi:10.1006/rwos.2001.0360.
- Barton, E., M. Inall, T. Sherwin, and R. Torres (2001), Vertical structure, turbulent mixing and fluxes during Lagrangian observations of an upwelling filament system off Northwest Iberia, *Prog. Oceanogr.*, *51*(2), 249–267.
- Bettencourt, J. H., C. Lopez, and E. Hernandez-Garcia (2012), Oceanic three-dimensional Lagrangian coherent structures: A study of a mesoscale eddy in the Benguela upwelling region, *Ocean Modell.*, *51*, 73–83, doi:10.1016/j.ocemod.2012.04.004.
- Bettencourt, J. H., C. Lopez, and E. Hernandez-Garcia (2013), Characterization of coherent structures in three-dimensional turbulent flows using the finite-size Lyapunov exponent, *J. Phys. A Math. Theor.*, *46* 254022, (1–20).

- Bettencourt, J. H., C. López, E. Hernández-García, I. Montes, J. Sudre, B. Dewitte, A. Paulmier, and V. Garçon (2015), Boundaries of the Peruvian oxygen minimum zone shaped by coherent mesoscale dynamics, *Nat. Geosci.*, *8*, 937–940, doi:10.1038/ngeo2570.
- Boffetta, G., G. Lacorata, G. Radaelli, and A. Vulpiani (2001), Detecting barriers to transport: A review of different techniques, *Physica D*, *159*(1–2), 58–70, doi:10.1016/S0167-2789(01)00330-X.
- Chapman, D. (1985), Numerical treatments of cross-shelf open boundaries in a barotropic coastal ocean model, *J Phys Oceanogr*, *15*, 1060–1075.
- Chenillat, F., B. Blanke, N. Grima, P. J. Franks, X. Capet, and P. Rivière (2015), Quantifying tracer dynamics in moving fluids: A combined Eulerian-Lagrangian approach, *Front. Environ. Sci.*, *3*, 43.
- Churchill, J. H., P. C. Cornillon, and G. W. Milkowski (1986), A cyclonic eddy and shelf-slope water exchange associated with a Gulf Stream warm-core ring, *J. Geophys. Res.*, *91*(C8), 9615–9623.
- Combes, V., F. Chenillat, E. D. Lorenzo, P. Rivière, M. Ohman, and S. Bograd (2013), Cross-shore transport variability in the California Current: Ekman upwelling vs. eddy dynamics, *Prog. Oceanogr.*, *109*, 78–89, doi:10.1016/j.pocean.2012.10.001.
- Cravo, A., P. Relvas, S. Cardeira, F. Rita, M. Madureira, and R. Sanchez (2010), An upwelling filament off southwest Iberia: Effect on the chlorophyll a and nutrient export, *Cont. Shelf Res.*, *30*, 1601–1613.
- da Silva, A., A. C. Young, and S. Levitus (1994), Atlas of Surface Marine Data 1994, Volume 1: Algorithms and Procedures, NOAA Atlas NESDIS 6, U.S. Dep. of Comm., Washington, D. C.
- Dee, D. P., et al. (2011), The ERA-Interim reanalysis: Configuration and performance of the data assimilation system, *Quart. J. R. Meteorol. Soc.*, *137*(656), 553–597, doi:10.1002/qj.828.
- d'Ovidio, F., V. Fernández, E. Hernández-García, and C. López (2004), Mixing structures in the Mediterranean Sea from finite-size Lyapunov exponents, *Geophys. Res. Lett.*, *31*, L17203, doi:10.1029/2004GL020328.
- d'Ovidio, F., J. Isern, C. López, E. Hernández-García, and E. García-Ladona (2009), Comparison between Eulerian diagnostics and Finite-Size Lyapunov Exponents computed from Altimetry in the Algerian basin, *Deep Sea Res., Part 1*, *56*, 15–31.
- Egbert, G., and S. Erofeeva (2002), Efficient inverse modeling of barotropic ocean tides, *J. Atmos. Oceanic Technol.*, *19*(2), 183–204.
- Fedorov, K., and A. Ginsburg (1989), Mushroom-Like Currents (Vortex Dipoles): One of the most widespread forms of non-stationary coherent motions in the ocean, in *Mesoscale/Synoptic Coherent structures in Geophysical Turbulence*, Elsevier Oceanogr. Ser., vol. 50, edited by J. Nihoul and B. Jamart, pp. 1–14, Elsevier, Amsterdam, doi:10.1016/S0422-9894(08)70173-9.
- Fennel, K., J. Hu, A. Laurent, M. Marta-Almeida, and R. Hetland (2013), Sensitivity of hypoxia predictions for the northern Gulf of Mexico to sediment oxygen consumption and model nesting, *J. Geophys. Res. Oceans*, *118*, 990–1002, doi:10.1002/jgrc.20077.
- Flather, R. (1976), A tidal model of the northwest European continental shelf, *Mém. Soc. R. Sci. Liège*, *6*, 141–164.
- García, D. (2010), Robust smoothing of gridded data in one and higher dimensions with missing values, *Comput. Stat. Data Anal.*, *54*(4), 1167–1178.
- Haidvogel, D. B., and A. Beckmann (1999), *Numerical Ocean Circulation Modeling*, Imperial College Press, London.
- Haidvogel, D. B., et al. (2008), Ocean forecasting in terrain-following coordinates: Formulation and skill assessment of the Regional Ocean Modeling System, *J. Comput. Phys.*, *227*(7), 3595–3624, doi:10.1016/j.jcp.2007.06.016.
- Haller, G. (2015), Lagrangian coherent structures, *Annu. Rev. Fluid Mech.*, *47*, 137–162.
- Haller, G., and G. Yuan (2000), Lagrangian coherent structures and mixing in two-dimensional turbulence, *Physica D*, *147*(3–4), 352–370, doi:10.1016/S0167-2789(00)00142-1.
- Haynes, R., E. D. Barton, and I. Pilling (1993), Development, persistence, and variability of upwelling filaments off the Atlantic coast of the Iberian Peninsula, *J. Geophys. Res.*, *98*(C12), 22,681–22,692.
- Hernandez-Carrasco, I., C. López, E. Hernández-García, and A. Turiel (2011), How reliable are Finite-Size Lyapunov Exponents for the assessment of ocean dynamics?, *Ocean Modell.*, *36*, 208–218.
- Hernández-Carrasco, I., V. Rossi, E. Hernández-García, V. Garçon, and C. López (2014), The reduction of plankton biomass induced by meso-scale stirring: A modeling study in the Benguela upwelling, *Deep Sea Res., Part 1*, *83*, 65–80.
- Hetland, R. D. (2006), Event-driven model skill assessment, *Ocean Modell.*, *11*, 214–223.
- Mancho, A. M., D. Small, and S. Wiggins (2006), A tutorial on dynamical systems concepts applied to Lagrangian transport in ocean flows defined as finite time data sets: Theoretical and computational issues, *Phys. Rep.*, *437*, 55–124.
- Marchesiello, P., J. C. McWilliams, and A. Shchepetkin (2001), Open boundary conditions for long-term integration of regional oceanic models, *Ocean Modell.*, *3*(1–2), 1–20, doi:10.1016/S1463-5003(00)00013-5.
- Marta-Almeida, M., J. Dubert, Á. Peliz, A. dos Santos, and H. Queiroga (2008), A modelling study of Norway lobster (*Nephrops norvegicus*) larval dispersal in southern Portugal: Predictions of larval wastage and self-recruitment in the Algarve stock, *Can. J. Fish. Aquat. Sci.*, *65*(10), 2253–2268, doi:10.1139/F08-138.
- Marta-Almeida, M., M. Ruiz-Villarreal, J. Pereira, P. Otero, M. Cirano, X. Zhang, and R. D. Hetland (2013a), Efficient tools for marine operational forecast and oil spill tracking, *Mar. Pollut. Bull.*, *71*(1–2), 139–151, doi:10.1016/j.marpolbul.2013.03.022.
- Marta-Almeida, M., R. D. Hetland, and X. Zhang (2013b), Evaluation of model nesting performance on the Texas-Louisiana continental shelf, *J. Geophys. Res. Oceans*, *118*, 2476–2491, doi:10.1002/jgrc.20163.
- Mellor, G. L., and T. Yamada (1974), A hierarchy of turbulent closure models for planetary boundary layers, *J. Atmos. Sci.*, *31*, 1791–1806.
- Meunier, T., V. Rossi, Y. Morel, and X. Carton (2010), Influence of bottom topography on an upwelling current: Generation of long trapped filaments, *Ocean Modell.*, *35*(4), 277–303.
- Nagai, T., N. Gruber, H. Frenzel, Z. Lachkar, J. C. McWilliams, and G.-K. Plattner (2015), Dominant role of eddies and filaments in the offshore transport of carbon and nutrients in the California current system, *J. Geophys. Res. Oceans*, *120*, 5318–5341, doi:10.1002/2015JC010889.
- Oey, L.-Y., and H. Zhang (2004), The generation of subsurface cyclones and jets through eddy-slope interaction, *Cont. Shelf Res.*, *24*(18), 2109–2131.
- Omand, M. M., E. A. D'Asaro, C. M. Lee, M. J. Perry, N. Briggs, I. Cetinić, and A. Mahadevan (2015), Eddy-driven subduction exports particulate organic carbon from the spring bloom, *Science*, *348*(6231), 222–225, doi:10.1126/science.1260062.
- Otero, P., M. Ruiz-Villarreal, and A. Peliz (2008), Variability of river plumes off north-west Iberia in response to wind events, *J. Mar. Syst.*, *72*, 238–255.
- Otero, P., M. Ruiz-Villarreal, Á. Peliz, and J. M. Cabanas (2010), Climatology and reconstruction of runoff time series in northwest Iberia: Influence in the shelf buoyancy budget off Ría de Vigo, *Sci. Mar.*, *74*(2), 247–266, doi:10.3989/scimar.2010.74n2247.
- Peliz, Á., T. L. Rosa, A. M. P. Santos, and J. L. Pissarra (2002), Fronts, jets, and counter-flows in the Western Iberian upwelling system, *J. Mar. Syst.*, *35*(1), 61–77.
- Prants, S. (2013), Dynamical systems theory methods to study mixing and transport in the ocean, *Phys. Scripta*, *87*(3), 038,115.

- Queiroga, H., T. Cruz, A. Dos Santos, J. Dubert, J. I. González-Gordillo, J. Paula, A. Peliz, and A. M. P. Santos (2007), Oceanographic and behavioural processes affecting invertebrate larval dispersal and supply in the Western Iberia upwelling ecosystem, *Prog. Oceanogr.*, *74*(2), 174–191.
- Relvas, P., E. D. Barton, J. Dubert, P. B. Oliveira, A. Peliz, J. Da Silva, and A. M. P. Santos (2007), Physical oceanography of the western Iberia ecosystem: Latest views and challenges, *Prog. Oceanogr.*, *74*(2), 149–173.
- Relvas, P., J. Luís, and A. Santos (2009), Importance of the mesoscale in the decadal changes observed in the northern Canary upwelling system, *Geophys. Res. Lett.*, *36*, L22601, doi:10.1029/2009GL040504.
- Rossi, V., Y. Morel, and V. Garçon (2010), Effect of the wind on the shelf dynamics: Formation of a secondary upwelling along the continental margin, *Ocean Modell.*, *31*(3–4), 51–79.
- Rossi, V., V. Garçon, J. Tassel, J.-B. Romagnan, L. Stemmann, F. Jourdin, P. Morin, and Y. Morel (2013a), Cross-shelf variability in the Iberian Peninsula Upwelling System: Impact of a mesoscale filament, *Cont. Shelf Res.*, *59*, 97–114.
- Rossi, V., M. Feng, C. Pattiaratchi, M. Roughan, and A. M. Waite (2013b), Linking synoptic forcing and local mesoscale processes with biological dynamics off Ningaloo reef, *J. Geophys. Res. Oceans*, *118*, 1211–1225, doi:10.1002/jgrc.20110.
- Santana-Falcón, Y., M. Benavides, P. Sangrá, E. Mason, E. D. Barton, A. Orbi, and J. Aristegui (2016), Coastal–offshore exchange of organic matter across the Cape Ghir filament (NW Africa) during moderate upwelling, *J. Mar. Syst.*, *154*(Part B), 233–242, doi:10.1016/j.jmarsys.2015.10.008.
- Shchepetkin, A. F., and J. C. McWilliams (2005), The regional oceanic modeling system (ROMS): A split-explicit, free-surface, topography-following-coordinate oceanic model, *Ocean Modell.*, *9*(4), 347–404, doi:10.1016/j.ocemod.2004.08.002.
- Sutyrin, G. G., and R. Grimshaw (2010), The long-time interaction of an eddy with shelf topography, *Ocean Modell.*, *32*(1), 25–35.
- Wallcraft, A. J., E. J. Metzger, and S. N. Carroll (2009), *Software Design Description for the HYbrid Coordinate Ocean Model (HYCOM) Version 2.2*, report number: NRL/MR/7320–09-9166, Naval Res. Lab., Stennis Space Cent., Hancock County, Miss.
- Zhang, X., R. D. Hetland, M. Marta-Almeida, and S. F. DiMarco (2012), A numerical investigation of the Mississippi and Atchafalaya freshwater transport, filling and flushing times on the Texas-Louisiana Shelf, *J. Geophys. Res.*, *117*, C11009, doi:10.1029/2012JC008108.